Shearless effective barriers to chaotic transport induced by even twin islands in nontwist systems

M. Mugnaine,[1,*] I. L. Caldas,[1] J. D. Szezech, Jr.,[2,3] R. L. Viana,[4] and P. J. Morrison[5]
[1]*Institute of Physics, University of São Paulo, São Paulo, São Paulo 05508-090, Brazil*
[2]*Graduate in Science Program—Physics, State University of Ponta Grossa, Ponta Grossa, Paraná 84033-240, Brazil*
[3]*Department of Mathematics and Statistics, State University of Ponta Grossa, Ponta Grossa, Paraná 84033-240, Brazil*
[4]*Department of Physics, Federal University of Paraná, Curitiba, Paraná 81531-980, Brazil*
[5]*Department of Physics and Institute for Fusion Studies, The University of Texas at Austin, Austin, Texas 78712, United States*

(Received 26 June 2024; accepted 13 September 2024; published 2 October 2024; corrected 29 October 2024)

For several decades now it has been known that systems with shearless invariant tori, nontwist Hamiltonian systems, possess barriers to chaotic transport. These barriers are resilient to breakage under perturbation and therefore regions where they occur are natural places to look for barriers to transport. Here we describe a kind of effective barrier that persists after the shearless torus is broken. Because phenomena are generic, for convenience we study the standard nontwist map (SNM), an area-preserving map that violates the twist condition locally in the phase space. The barrier occurs in nontwist systems when twin even period islands are present, which happens for a broad range of parameter values in the SNM. With a phase space composed of regular and irregular orbits, the movement of chaotic trajectories is hampered by the existence of shearless curves, total barriers, and a network of partial barriers formed by the stable and unstable manifolds of the hyperbolic points. Being a degenerate system, the SNM has twin islands and, consequently, twin hyperbolic points. We show that the structures formed by the manifolds intrinsically depend on period parity of the twin islands. For this even scenario the structure that we call a torus free barrier occurs because the manifolds of different hyperbolic points form an intricate chain atop a dipole configuration and the transport of chaotic trajectories through the chain becomes a rare event. This structure impacts the emergence of transport, the escape basin for chaotic trajectories, the transport mechanism, and the chaotic saddle. The case of odd periodic orbits is different: we find for this case the emergence of transport immediately after the breakup of the last invariant curve, and this leads to a scenario of higher transport, with intricate escape basin boundary and a chaotic saddle with nonuniformly distributed points.

DOI: 10.1103/PhysRevE.110.044201

I. INTRODUCTION

The analysis of a Hamiltonian system can be reduced to area-preserving maps, symplectic maps that arise as canonical Poincaré maps for systems of differential equations [1,2]. Near-integrable Hamiltonian systems possess a phase space with coexistence of regular and irregular (chaotic) orbits. The questions of where chaotic trajectories go and how long they take to move from one region of the phase space to another naturally emerge, and are the subject of a large literature on transport theory (see, e.g., Refs. [3,4]). Transport theory concerns the collective movement of chaotic trajectories and includes techniques for estimating the transport rates, which can be related to quantities in experiments [5]. Transport analysis has application in many research fields, such as plasma confinement [6,7], fluid dynamics [8,9], and celestial mechanics [10,11].

Hamiltonian systems possess an intermixture of periodic, quasiperiodic, and chaotic orbits and the movement of the irregular components can be affected by partial barriers and remnants of invariant tori, the cantori [3,4]. A cantorus is an invariant set with irrational frequencies formed by an infinite number of gaps [6], which can provide a robust partial barrier in the phase space. The existence of cantori in the phase space has only been proven for nondegenerate systems, i.e., systems where the frequency of the motion on a torus is related with the action of the torus by a monotonic function (see, e.g., Refs. [9,12]). Maps with this monotonic behavior are called twist maps, and the Kolmogorov-Arnold-Moser (KAM) theorem and Aubry-Mather theory can be applied since the twist condition, defined for maps as $\partial x_{n+1}/\partial y_n \neq 0$, is satisfied at every point in the phase space [13,14]. A map that violates such conditions is called nontwist and its universal behavior can be described by the standard nontwist map (SNM) given in Ref. [9], the simplest mathematical model that violates the twist condition.

Even though the existence of cantori has not been proven for nontwist maps and the conventional KAM theorem cannot be applied at every point of the phase space, there are rigorous KAM results for nontwist maps [15]. Moreover, transport has been widely studied in nontwist systems (e.g., Refs. [16–24]). In the SNM, depending on parameter values, the phase space can be composed of a chaotic sea bounded by invariant curves with two chains of islands immersed in the chaotic regions. Due to the violation of the twist condition, the two chains of islands are twins; i.e., they have the same frequency but are not connected [25,26]. Among the invariant curves, there

*Contact author: mmugnaine@gmail.com

is the shearless curve formed by the points where the twist condition is violated. The shearless curve is also the extremum point of the nonmonotonic frequency function. In a transport portrayal, the shearless curve acts as a barrier; i.e., it divides the chaotic sea into two regions, thereby preventing global transport. Thus, the transition to global chaos is related to the destruction of this barrier as was first investigated by Greene's method in Ref. [13].

After the shearless curve breaks, chaotic orbits can be limited by the existence of partial barriers. As noted in Ref. [19], there can be an effective barrier formed by the remnants of the shearless curve, which trap the chaotic orbits. There is also the phenomenon of stickiness around the twin islands. The manifolds also have an important role in creating the partial barriers [16,27], since the intra-intercrossing scenario, represented by the homoclinic-heteroclinic intersections of the manifolds, has an effect on the transport intensity. Interestingly, the transport studies of these earlier works were performed for the standard nontwist map with island chains of odd period. Due to the map symmetries, the relative positions of the islands change for different parity. For the odd case, a hyperbolic and an elliptic orbit are aligned, while for the even case two elliptic points are aligned. Because there is no dynamical manifold based description for the scenario of partial barriers with islands of even period, we provide numerical evidence for characterizing the behavior. Our characterization of these partial barriers yields an explanation for zero and low transport for certain parameters of the SNM.

In our numerical survey of the SNM we analyze even and odd scenarios and compare the transport mechanisms acting in the two cases. We show that for the even scenario, the transport of chaotic trajectories is obstructed by a network formed by the stable and unstable manifolds related to the chains of hyperbolic points. We called this network structure a torus free barrier (TFB), since there is no invariant curve, but the transport rarely happens due to the manifold configuration. These results can be generalized for more complex degenerate Hamiltonian systems with the same structures of twin island chains.

Our paper is organized as follows: In Sec. II we present the standard nontwist map and discuss features of the phase space related to the parity of the islands. We also discuss the nonmonotonic behavior of the frequency function. Transmissivity through the phase space is discussed in Sec. III. Here we investigate the escape of chaotic trajectories from the escape basin and measure their escape times. In Sec. IV, we describe the TFB structure that is responsible for the null or low transport of the system. Then, in Sec. V we further analyze the transport through the TFB, explaining the rarity of such transport of a chaotic trajectory. Finally, in Sec. VI we conclude.

II. PARITY SCENARIOS FOR THE STANDARD NONTWIST MAP

The standard nontwist map is an area-preserving map that was obtained from a Hamiltonian model that describes transport and mixing properties of Rossby waves in zonal shear flows [9]. It also arises from a model for the motion of charged particles in drift waves in confined plasmas [7]. The map is given by

$$\begin{aligned} y_{n+1} &= y_n - b\sin(2\pi x_n), \\ x_{n+1} &= x_n + a\left(1 - y_{n+1}^2\right), \quad \mod 1, \end{aligned} \tag{1}$$

where the canonically conjugate variables are $y \in \mathbb{R}$ and $x \in [0, 1]$. The parameters a and b are real and independent of each other, and the domain of interest is $a \in [0, 1]$ and $b \in \mathbb{R}$. The map violates the twist condition, $\partial x_{n+1}/\partial y_n \neq 0$, at points in the phase space which belong to the so-called shearless curve. This map was first thoroughly studied in Refs. [13,28], where the breakup and scaling of the shearless curve were analyzed.

For $b \neq 0$ the SNM represents a nonintegrable Hamiltonian system with a phase space with coexistence of chaotic and regular solutions. The shearless curve is a quasiperiodic solution represented by a curve that spreads across the whole domain of x. There are also quasiperiodic orbits that wind around stable periodic solutions. These orbits constitute the islands and, due to the violation of the twist condition and the symmetry of the map, they come in pairs adjacent to the shearless curve [28,29].

The search for periodic solutions can be reduced to a one-dimensional problem since the map (1) can be factored in two involutions, i.e.,$M = I_1 I_0$, where $I_{0,1}$ are time-reversal symmetries [13]. In the SNM, the primary periodic stable orbits (elliptic points) are always on one of the symmetry lines, defined by $I_{0,1}\mathbf{x} = \mathbf{x}$, which results in

$$\begin{aligned} s_0 &= \{(x, y)|x = 0\}, \\ s_1 &= \{(x, y)|x = a(1 - y^2)/2\}. \end{aligned} \tag{2}$$

Thus, the search for stable periodic orbits is a root-finding problem along these lines. The symmetry properties of the SNM are due to the symmetry transformation $T_S(x, y) = (x + \frac{1}{2}, -y)$, with which the relation $M_{SNM}T_S = T_S M_{SNM}$, with M_{SNM} defined by Eqs. (1), is valid. The symmetry transformation can be applied to the symmetry lines in Eqs. (2), and two other lines can be found:

$$\begin{aligned} s_2 &= \{(x, y)|x = 1/2\}, \\ s_3 &= \{(x, y)|x = a(1 - y^2)/2 + 1/2\}. \end{aligned} \tag{3}$$

As mentioned, the periodic orbits in the map come in pairs; i.e., there are two periodic solutions with the same frequency, one on each side of the shearless curve [28]. According to the period parity of the periodic orbits, their relative positions are different if the period is even or odd. For a scenario where the periodic orbits exhibit even period, the fixed points of the same stability, of each chain of islands, belong to the same symmetry line, while for odd period, the points with opposite stability are aligned along the symmetry line. In order to illustrate this, we compute phase-space plots for the SNM with islands of period 2 and 3, along with the four symmetry lines defined by Eqs. (2) and (3). The plots are shown in Fig. 1.

In Fig. 1 we have phase-space plots for the even and odd scenarios along with the symmetry lines s_i, for $i = 0, 1, 2$, and 3 from Eqs. (2) and (3). The symmetry lines s_0 and s_2 are the vertical dashed lines at $x = 0$ and $x = 0.5$, respectively, while the lines s_1 and s_3 correspond to the left and right dashed parabolas. For the even scenario, we chose $a = 0.53$ and $b = 0.45$ for Fig. 1(a) and $b = 0.53$ for Fig. 1(c). In the

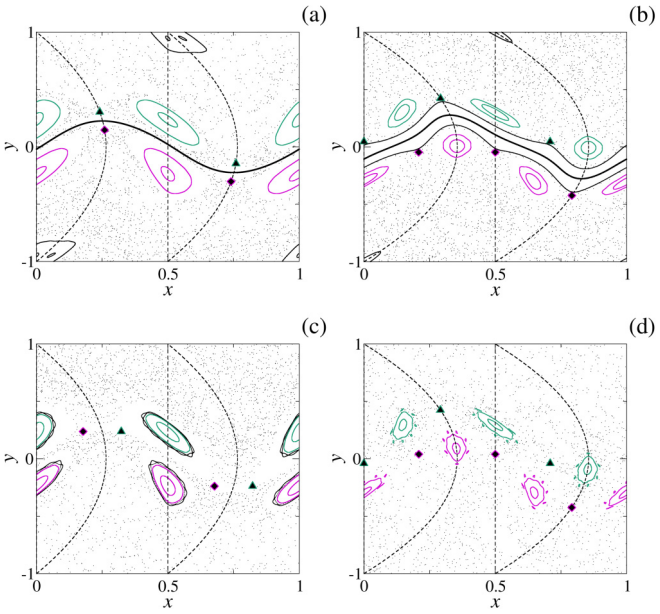

FIG. 1. Phase-space plots for the even and odd scenarios. In (a) and (c) we choose $a = 0.53$ and for (b) and (d), $a = 0.71$. The islands are represented by the colored closed curves, the hyperbolic points by the triangle and diamond symbols, and the shearless curve, when it exists, by the thick curve. The even scenario before the breakup of the shearless curve is shown in (a) for $b = 0.45$, while the odd scenario with the curve is represented in (b) for $b = 0.39$. In (c) and (d), we choose $b = 0.53$ and $b = 0.48$ in order to represent the even and odd scenarios after the breakup of the shearless curve, respectively.

phase-space plots for the odd scenario, we have $a = 0.71$ and $b = 0.39$ for Fig. 1(b) and $b = 0.48$ for Fig. 1(d).

In Fig. 1(a), the islands have period 2, and they are indicated by the colored closed curves. We indicate the islands as upper and lower island chains with different colors: the upper (lower) chain in green (magenta) is in the upper (lower) side of the shearless curve, represented by the thick black curve in the center. In Fig. 1(a), we observe elliptic points on the same symmetry lines s_0 and s_2 while the hyperbolic points, represented by the triangle and diamond symbols, are also in the same line, but in this case s_1 and s_3. The scenario for odd period is quite different. As seen in Fig. 1(b), in the same symmetry line we have an elliptic and a hyperbolic point.

When the shearless curve no longer exists, we have the phase-space plots of Figs. 1(c) and 1(d), for the even and odd scenarios, respectively. In Fig. 1(d), we observe the same behavior seen in Fig. 1(b) when the curve was present: the elliptic and hyperbolic points are aligned along the symmetry line. This is not observed for the even scenario. Though the elliptic points are still aligned in Fig. 1(c), the hyperbolic points are not on the symmetry lines and, consequently, the two chains of hyperbolic points are no longer related by the symmetry transformation T_S. This happens because, when the collision of hyperbolic points occurs at the shearless breakup, they scatter in a direction transverse to the symmetry line. For a detailed discussion about the collision, see Ref. [13].

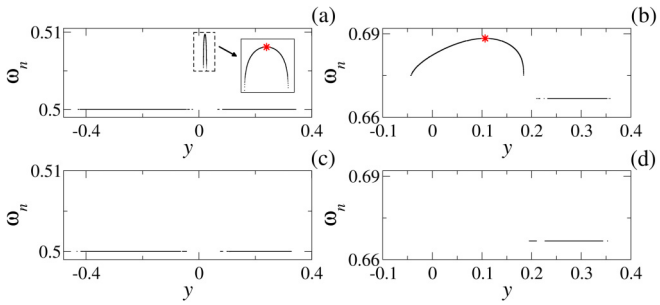

FIG. 2. Winding number profiles computed along the symmetry line $x = 0.5$ for the phase-space plots of Fig. 1. The parameters a and b for (a)–(d) are the same as those for Figs. 1(a)–1(d), respectively. The red stars indicate the maximum value of ω_n in (a) and (b). The magnification in (a) is around the region framed by the dashed box.

The thick curves in Figs. 1(a) and 1(b) are the shearless curves, the set of points where the twist condition is violated and the winding number assumes an extreme value. The winding number of an orbit, also called the rotation number, is defined by the limit

$$\omega_n = \lim_{n\to\infty} \frac{x_n}{n}, \tag{4}$$

which converges to a rational (irrational) value for a periodic (quasiperiodic) orbit. Limit (4) does not converge if the orbit is chaotic. Computing the winding number profiles along the symmetry line $s_2 : x = 1/2$ for the phase-space plots of Fig. 1, we have the profiles shown in Fig. 2.

For the winding number profiles of Fig. 2, we compute limit (4) for 10^5 initial conditions on the symmetry line $x = 1/2$ with a final iteration time $n = 10^6$. Observing the phase-space plots of Fig. 1, the majority of the solutions on the symmetry line are chaotic and they do not have a defined ω_n. For this reason, the domain of y used for the winding number profiles is reduced to $y \in [-0.4, 0.4]$ for Figs. 2(a) and 2(c), the even scenario, and $y \in [-0.1, 0.4]$ for Figs. 2(b) and 2(d), the odd scenario.

The even scenario with shearless curve is shown in Fig. 2(a), with $a = 0.53$ and $b = 0.38$. The profile ω_n is composed of two plateaus at $\omega_n = 0.5$ indicating the two islands of period 2. Between these two plateaus, we observe nonmonotonic behavior of the winding number, highlighted by the magnification: a parabola with the extreme point indicating the position of the shearless curve. The points on the left and right of the maximum point are due to other curves that occupy the whole domain of x and are not shown in Fig. 1(a). Similar behavior is observed in Fig. 2(b), but in this case, we only observe one plateau at $\omega_n = 1/3$, representing the upper island of period 3. This difference is due to the disposition of the islands in the symmetry lines as discussed before. Since the elliptic points are aligned along the symmetry line for the even case, we observe two plateaus, differently from the odd scenario where the hyperbolic point is aligned with the elliptic point and only one plateau can be seen.

Figures 2(c) and 2(d) represent the even and odd scenario for $(a, b) = (0.53, 0.53)$ and $(a, b) = (0.71, 0.48)$, respectively. For these parameters, the shearless curve no longer exists and, in both profiles, only the plateaus remain,

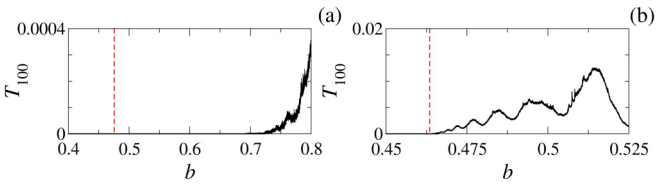

FIG. 3. Transmissivity profile for the SNM with (a) $a = 0.53$, representing the even scenario, and (b) $a = 0.71$, representing the odd case. The red dashed line indicates the b value for the breakup of the shearless curve.

indicating the persistence of the islands with the increasing of the perturbation amplitude b. Once again, we can observe two plateaus for the even case and just one for the odd scenario.

In this work we restrict our analysis to a shear profile with one extremum point, i.e., one shearless curve and a pair of twin islands, symmetrically placed on each side of the shearless curve. Profiles with this symmetry broken or more extremum points are of interest. With more extremum points, where symmetry could be broken, we would see more shearless curves and eventually more islands. The manifold structures of such scenarios are yet to be determined.

III. TRANSPORT ACROSS THE PHASE SPACE

As observed in Figs. 1(a) and 1(b), the shearless curve acts as a barrier to transport, since it divides the chaotic sea into upper and lower regions. Thus, the transition to global chaos and, consequently, global transport requires the destruction of the shearless barrier [13]. For some set of parameters (a, b) where the shearless curve no longer exists, chaotic solutions can cross the phase space, leading to high transport. In order to quantify and describe the transport through the phase space, we use the transmissivity quantifier and the concepts of escape time and escape basins.

A. Transmissivity

The transmissivity is a quantifier defined as the fraction of orbits that cross a region of the phase space in a predefined time interval [19]. Numerically, we randomly choose $N_T = 10^6$ initial conditions on the line $y = -2.0$, iterate all of them for 100 iterations, and compute how many cross the phase space and reach the line $y = 2.0$. The fraction is the transmissivity T_{100}. As performed before, we compute the quantifier for two scenarios: even and odd. For the even scenario we again choose $a = 0.53$ and for the odd, $a = 0.71$. The behavior of T_{100} relative to the perturbation parameter b is shown in Fig. 3.

From the transmissivity profiles in Fig. 3, we can affirm that transport across phase space with islands of even period differs from that with islands of odd period. The b values for the breakup of the shearless curve are indicated by the red dashed lines: $b \approx 0.4754$ and $b \approx 0.4635$ for Figs. 3(a) and 3(b), respectively. In the even scenario, represented by the profile in Fig. 3(a), we observe that, even without a barrier, the transport can be null for a large range of parameters for 100 iterations. The shearless curve breaks at the point $b \approx 0.4754$ but a non-null transport in 100 iterations is noticed only for $b = 0.70$. In contrast is the result observed in Fig. 3(b) where the islands in the phase space have odd period. In this case, the transport is non-null right after the shearless breakup. Therefore, for the even scenario, we have a transport barrier without an actual barrier, a TFB.

In order to investigate the difference between no or low transport for the even case and the higher transport for the odd case for a certain iteration time, we analyze the phase space and the chaotic solutions for some values of b. We choose two values of b for the even case, one for the scenario with a TFB and another for the higher transport observed in Fig. 3(a), therefore, $b = 0.53$ and $b = 0.80$, respectively. For the odd case, we analyze the peak of transport for $b = 0.494$ of the transmissivity profile of Fig. 3(b). We examine the three sets of parameters using the concepts of escape basin and escape time, stated in the next section.

B. Escape basins and escape time

Consider now how the chaotic solutions distributed over the phase space behave during the time evolution of the map. For this, we unite the escape time and the escape basin analysis, since we can set exits in the phase space of the SNM. The escape basin associated with an exit is the set of points which escape through this exit within a time interval, while the escape time is the number of iterations a solution takes to go through the exit.

As in previous studies (see Refs. [16–18,30]), we define two exits in the phase space: the lines $y = \pm 1.0$. Then we uniformly distribute $2.10^3 \times 2.10^3$ initial conditions in the domain $\mathcal{D} : \{(x, y)|x \in [0, 1] \text{ and } y \in [-1, 1]\}$ and iterate all of them for 10^3 iterations. During the time evolution, if the solution crosses one of the two exits $y = \pm 1$ we record which exit and also the iteration number at which the crossing happens. We join these two pieces of information in a color scale for the phase space. If the solution crosses the exit $E^+ : y = +1$ ($E^- : y = -1$), we set its initial condition as a green (pink) point in the phase space. The shade of green and pink is related to the escape time: the darker it is, the longer the escape time. The escape basins and the escape times for $(a, b) = (0.53, 0.53)$, $(a, b) = (0.53, 0.80)$, and $(a, b) = (0.71, 0.494)$ are shown in Fig. 4.

Figure 4(a), with $(a, b) = (0.53, 0.53)$, represents the even scenario with a TFB, while Fig. 4(b) shows the peak of transport for the even scenario of Fig. 3(a), with $(a, b) = (0.53, 0.80)$. For both cases of Figs. 4(a) and 4(b), we observe a smooth boundary between the green and the pink basins; i.e., there is no significant mixing between the two colored regions. Thus, the trajectories which begin in the lower or upper region of the phase space tend to escape through the lower or upper exit and, consequently, crossing the phase space is a rare event. A different outcome is seen in the odd scenario of Fig. 4(c), where the boundary between the basins is no longer smooth. In fact, the boundary is intricate and there is a mixing region of the pink and green points around the islands (the islands are indicated by the white regions). This mixing leads to a greater uncertainty, since close initial conditions can escape through different exits. From the result presented in Fig. 4(c), we can also affirm that the crossing through the phase space is

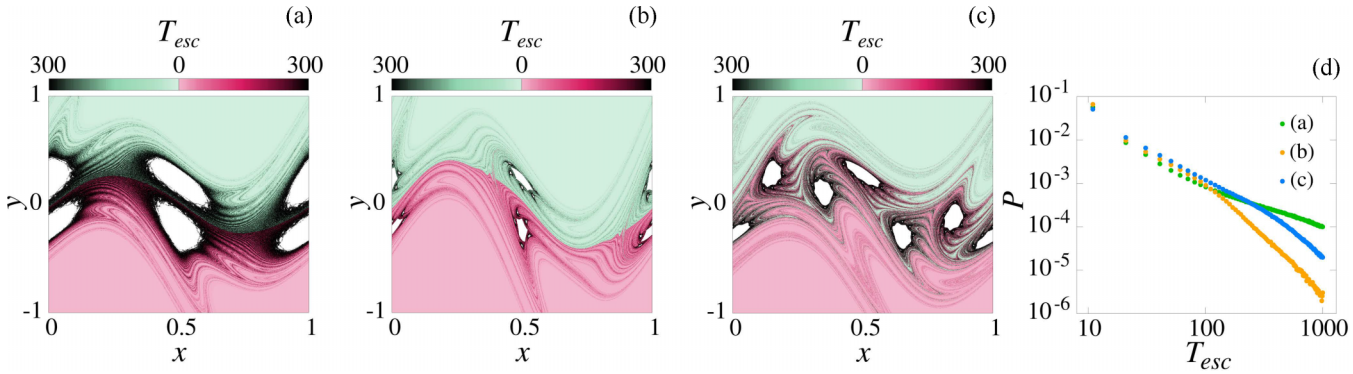

FIG. 4. Escape time and escape basin for the SNM for the even scenario with $a = 0.53$, (a) $b = 0.53$ and (b) $b = 0.80$, and for the odd scenario, with (c) $(a, b) = (0.71, 0.494)$. The pink (green) points indicate the initial condition of the solution, which cross the exit E^- : $y = -1.0$ (E^+ : $y = +1.0$) within 10^3 iterations. The color shade, as shown in the color bar, indicates the escape time: light pink or green indicates a small escape time while the darker points indicate longer escape times. (d) The respective escape time distributions for the three scenarios.

more common, comparing to the case in Fig. 4(b), since there are green and pink points in the lower and upper regions.

From Fig. 4, we observe that greater escape times happen for trajectories with initial conditions near the islands. This is due to the stickiness phenomenon; i.e., chaotic solutions get stuck around the quasiregular orbits for a certain time interval. Figure 4(a) presents the larger black region, indicating a stronger stickiness in this case. For Figs. 4(b) and 4(c), we observe a more restrained stickiness region around the islands. The majority of the escape basins present light shades of pink and green, indicating a short escape time. The darker shades are closer to the islands and, apparently, distance themselves from the islands in patterns that resemble manifolds. Therefore, it seems the manifolds reflect the behavior of the chaotic solutions and their transport through the phase space.

In order to verify the presence of stickiness in the phase space, we compute the distributions for the escape times of Figs. 4(a)–4(c) shown in Fig. 4(d). For the distributions, we chose 1000 iterations as the final time. In general, the presence of stickiness affects the temporal quantifier distributions, such as the distribution of escape times [31,32], recurrence times [33], trapping times [34], and others. From the time distributions presented in Fig. 4(d), we find the decay exponents presented in Table I.

From the analysis performed above, we identify a power-law decay for all cases. We claim this happens because the stickiness phenomenon occurs in all phase spaces, as discussed before. The exponent for the scenario shown in Fig. 4(a) is smaller in modulus, indicating that the decay takes a longer time to occur. This result is in agreement with the larger black region in around the islands. Comparing the decays with the black regions around the islands, we can conclude that the smaller the exponent in modulus the greater the black region, i.e., the stickinnes region in the phase space.

TABLE I. Decay exponents for the power laws related to the distribution times of Fig. 4(d).

Escape time distribution	Decay parameter
Fig. 4(a)	-0.921 ± 0.006
Fig. 4(b)	-2.50 ± 0.02
Fig. 4(c)	-1.76 ± 0.02

IV. TORUS FREE BARRIERS

Transport analyses aim to characterize the motion of chaotic trajectories through phase space (e.g., Ref. [4]). Typically nonintegrable Hamiltonian systems that are perturbations of integrable ones have a coexistence of chaos and regularity, with islands and invariant curves that can affect, limit, and/or preclude transport. The Poincaré-Birkhoff theorem states that for each elliptic fixed point at the center of the islands there corresponds unstable hyperbolic fixed points in the chaotic sea. As shown in Refs. [16,19,20,27], the stable and unstable manifolds related to the hyperbolic points impact the transport of chaotic trajectories in the SNM. Following this idea in the present context, we perform a numerical study about the manifolds, for the phase-space plots of Fig. 4, in order to explain the torus free barrier scenario and the peaks of transmissivity through the phase space.

Let $\mathbf{O}^{\blacktriangle}(\mathbf{O}^{\blacklozenge})$ denote the hyperbolic points of the upper (lower) island chain and denote its unstable and stable manifolds by $W_u^{\blacktriangle}(W_u^{\blacklozenge})$ and $W_s^{\blacktriangle}(W_s^{\blacklozenge})$, respectively. The crossing between stable and unstable manifolds can form an intracrossing scenario, where we have homoclinic intersections formed by the crossings between manifolds of the same chain of hyperbolic points. We can also observe an intercrossing scenario, where the crossings are between the manifolds of different chains of hyperbolic points, resulting in heteroclinic intersections [16,19]. For the phase-space plots of Fig. 4, the stable and unstable manifolds of each chain of hyperbolic points are shown in Fig. 5.

Figure 5 depicts the stable and unstable manifolds related to hyperbolic points of the SNM for the same parameters as those of Fig. 4. In Fig. 5(a) the manifolds are shown for the case of the TFB, where we have no transport without a total barrier. The blue and pink curves, representing $W_s^{\blacktriangle}$ and $W_u^{\blacklozenge}$, respectively, surround the two islands in a dipolelike shape and the crossing structure between these two manifolds resembles the usual turnstile or homoclinic structure. The intriguing and newly observed structure is the one formed by the green and orange curves, the stable and unstable manifolds

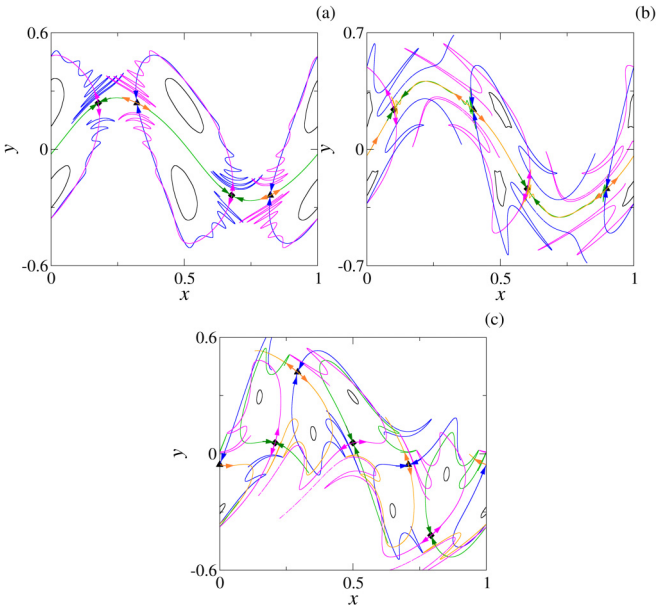

FIG. 5. Manifold structure for the phase-space plots of Fig. 4. The upper (lower) hyperbolic points $\mathbf{O}^{\blacktriangle}$ ($\mathbf{O}^{\blacklozenge}$) are represented by the triangle (diamond) symbol. The manifolds $W_s^{\blacktriangle}$, $W_s^{\blacklozenge}$, $W_u^{\blacktriangle}$, and $W_u^{\blacklozenge}$ are indicated by the blue, green, orange, and pink curves. Close to the hyperbolic points, we draw arrows indicating the stability direction: inwards and outwards, indicating the stable and unstable directions of the hyperbolic point.

of the lower and upper chain, $W_u^{\blacktriangle}$ and $W_s^{\blacklozenge}$, respectively. These two manifolds are apparently superimposed and form what appears to be a smooth curve across the interior of and between the dipoles. This smooth curve corresponds to the smooth boundary between the two escape basins of Fig. 4(a). From our numerical simulations, we claim that there are no manifolds that connect hyperbolic points from different chains in the region inside and outside of the dipole. Even though it seems the manifolds occupy the same region, in the region outside the dipole, the green curve oscillates and moves away from the triangle hyperbolic point $\mathbf{O}^{\blacktriangle}$. The same happens with the orange curve: it gets closer to the diamond point $\mathbf{O}^{\blacklozenge}$, but then the manifold follows the pink manifolds and moves away from the point. In the curve inside the dipole, there are small oscillations and, consequently, crossings between the green and orange curves. (The crossings are shown in the magnification given in Fig. 6.)

At the peak of transmissivity of Fig. 3(a) we have $(a, b) = (0.53, 0.8)$; the corresponding manifolds are presented in Fig. 5(b). We observe a structure similar to the one presented in Fig. 5(a), but the crossings between the orange and green curves are more evident. These crossings form lobes and enable chaotic orbits to cross the phase space at these regions. Thus, the TFB structure is modified and the transport through the phase space is higher.

For the odd scenario, presented in Fig. 5(c), we have the usual turnstile structure. This is a well-known case already investigated and described in the literature [4,16]. The peak of transmissivity for this phase-space structure is due to the intercrossing between the manifolds of different chains of hyperbolic points. For a more complete description of how

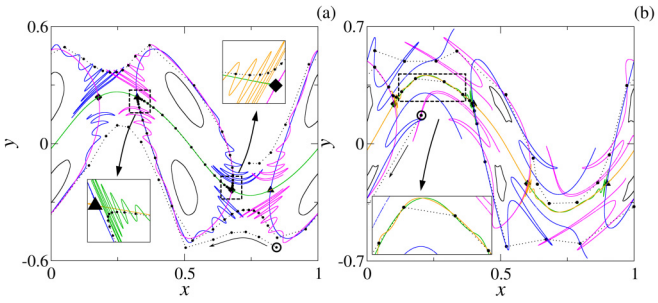

FIG. 6. Transport of a chaotic trajectory through the dipolelike configuration. The initial condition of the orbit is highlighted with a circumference and the direction of the orbit is indicated by arrows. In (a), we have $b = 0.53$ representing the scenario where the transport is a very rare event while in (b), $b = 0.8$, we have the peak of transmissivity of the profile in Fig. 3(a). The manifold color scheme is the same as that of Fig. 5. The insets in each panel are magnifications of the corresponding regions inside the dashed squares.

the intercrossing is responsible for an increase in the transport see Ref. [16].

V. TRANSPORT MECHANISM

As noted above, the manner in which trajectories traverse phase space for the odd scenario case has been well studied, including its understanding in terms of conventional turnstiles. However, to our knowledge, the manner in which trajectories cross the dipolelike configuration for the even scenario case has not been previously investigated. For the even case when TFBs exist, because they are not perfect barriers, transport can occur; however, our numerical simulations show that this is rare and the number of iterations needed is large. For example, for the phase-space plot of Fig. 5(a), fewer than 0.01% of the trajectories cross the phase space in 10^5 iterations. Thus, the TFB is a partial but quite strong transport barrier.

In order to understand the transport mechanism, we search for trajectories that cross the phase space and analyze their behavior inside the dipolelike structure. In particular, we analyze the transport through the structures shown in Figs. 5(a) and 5(b). Our results are shown in Fig. 6, where we trace trajectory paths through the twin island chain region. We consider representative initial conditions, highlighted by circles, and consider the same parameters a and b of Figs. 5(a) and 5(b), respectively. In Fig. 6(a) an escape path is seen by following the arrows indicating the direction of the trajectory. We observe that the trajectory crosses the TFB inside the dipolelike configuration. In contrast, in Fig. 6(b) we see the crossing happens in the region between the two dipoles. The magnifications of the insets show how the crossing happens: the trajectory goes from the lower part of the phase space to a region inside a lobe formed by the green and orange manifold, and then stays inside the lobes upon each iteration. Then, due to the crossings between these manifolds, the trajectory goes to the upper region of the phase space. These scenarios occur for both phase-space plots shown in Fig. 6.

As discussed in Ref. [3], there is a relationship between the area of the lobes formed by the stable and unstable manifolds and the flux of trajectories through phase space. Therefore,

we can explain the low and high transport in the phase spaces of Figs. 6(a) and 6(b), respectively, by the area of the lobes formed by the manifolds. In Fig. 6(a), the lobes formed by the green and orange manifolds are exceptionally small and can only be seen in the magnifications. Furthermore, they are restricted to the region inside the dipole region. The combination of small size with the restriction of being only inside the dipoles is the reason the crossing of chaotic trajectories is a rare event in this configuration. For the different escape path of Fig. 6(b), where the transport is higher, we can observe the lobes formed by the crossings without any magnification; i.e., they are significantly bigger in size. In summary, the lobes between the dipoles boost the transport of chaotic trajectories in the phase space, due to their size and, consequently, the area inside them.

As is well known, the stable and unstable manifolds are nonattracting invariant sets that play a fundamental role in the dynamics of the chaotic systems [35]. The results of Figs. 5 and 6 support this idea. Hence, we study a nonattracting invariant set as a *chaotic saddle*. Let $\mathcal{R}$ be a limited region in the phase space; in our case $\mathcal{R}$ is the domain $\mathcal{D} := \{(x, y)|x \in [0, 1] \text{ and } y \in [-1, 1]\}$. There is a set of points which remain in $\mathcal{R}$ for all time under forward iteration of the SNM, and another set of points remains in the region for all time under the backward iteration of the map. These sets are the stable and unstable sets, respectively, and their union is the chaotic saddle [36]. We compute an approximation of the chaotic saddle by the "sprinkler method" proposed in Ref. [35]. The method consists of placing points on a fine grid over the region $\mathcal{R}$ and iterating all the points until a final iteration n_F. The initial conditions of the trajectories that stay in the region during all the iterations approximate the stable set, their final positions approximate the unstable manifold, and the iteration $n_F/2$ approximates the chaotic saddle.

To calculate the chaotic saddle for the phase-space plots of Fig. 5, we use a grid of 2000×2000 initial conditions in $\mathcal{D}$, discard points that belong to the islands, and consider the final iteration $n_F = 100$. The chaotic saddle is shown in Fig. 7. From Fig. 7 and the value of the transmissivity for each of the cases of Fig. 5, we can confirm that there is a relationship between the spatial distribution of the invariant set and the transport through the phase space. The saddle of Fig. 7(a) is related to the case with the TFB: here the chaotic saddle is dense and distributed in the whole domain of x. Visually, the density appears uniform on the whole saddle. A different scenario is observed in Fig. 7(b). In this case, we observe that the chaotic saddle is denser around the island of period 2 and the saddle has "holes" and "channels," i.e., paths for the chaotic orbits to cross the phase space with no restriction. Lastly, the chaotic saddle for the odd scenario, Fig. 7(c), is dense around the islands but we can also observe the channels inside the saddle. With these results, it seems that a uniformly distributed and continuum saddle is related to a scenario with small transport through the phase space, while the saddles that are not uniformly distributed and are subdivided can lead to a scenario with non-null transport.

As an additional analysis to differentiate the chaotic saddles of Fig. 7, we compute the box counting dimension D_0 for each saddle. The dimension D_0 is also called the capacity dimension, Hausdorff dimension, or, more generically,

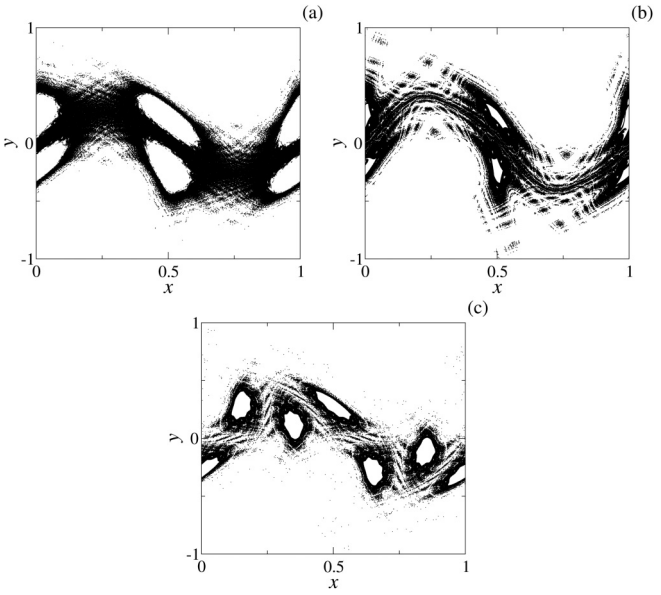

FIG. 7. Approximation of the chaotic saddle correspondent to the phase spaces of Fig. 5. The computation is made in a grid of 2000×2000 initial conditions $n_F = 100$. The black points represent the iteration $n = 50$ for orbits that do not escape the region $\mathcal{D} : \{(x, y)|x \in [0, 1] \text{ and } y \in [-1, 1]\}$ in 100 iterations.

the fractal dimension [37], and it is defined by

$$D_0 = \lim_{\epsilon \to 0} \frac{\log N(\epsilon)}{\log\left(\frac{1}{\epsilon}\right)}, \tag{5}$$

where $N(\epsilon)$ is the minimum number of boxes of side ϵ needed to cover the object, in our case the chaotic saddle. Computing the fractal dimension for each chaotic saddle of Fig. 7, we obtain the values presented in Table II.

Comparing the values of D_0 presented in Table II with the decay exponents of Table I, we can observe a relation between both measures. Longer decays, i.e., greater exponents in modulus, are related to chaotic saddles with greater dimension. From our results shown above, saddles with greater (lower) dimension present fewer "channels" and, consequently, fewer (more) ways to escape.

VI. CONCLUSIONS

The transport of chaotic trajectories across the phase space is prevented in nontwist Hamiltonian systems by the existence of the shearless curve, an invariant set that is robust to strong perturbations. After the shearless curve breakup, the transport

TABLE II. Box counting dimension for the chaotic saddles of Fig. 7.

Chaotic saddle	Box counting dimension
Fig. 7(a)	1.769 ± 0.007
Fig. 7(b)	1.63 ± 0.03
Fig. 7(c)	1.69 ± 0.02

is affected by the structures formed by the stable and unstable manifolds related to the twin chains of hyperbolic points. We analyzed the transport in nontwist systems by using the paradigmatic standard nontwist map, and we observed that the parity of the twin islands plays a crucial role in the collective motion of chaotic trajectories. For even period islands the transport can be null for a predefined iteration time, even though there is not a complete barrier, while for the odd scenario we observe the emergence of transport immediately after the shearless curve breakup.

Besides the transmissivity, the parity of the islands also affects the escape basin and the relative escape times. For the odd case, we observe an intricate boundary between the escape basins. Additionally, the escape times are notably longer, which can be attributed to the stickiness and the hierarchy of the islands around the islands' structure. The boundary between the escape basin is smooth for the even case, and the escape times are related to the manifold structure that emerges in the even scenario case.

We justified the difference between the transport for the even and odd cases by examining the structures formed by the manifolds related to the chains of hyperbolic points. For the odd case, we saw the well-known structure of manifolds that can act like turnstiles for the chaotic trajectories. The main novelty of the present paper is the structure formed by the manifolds in the even scenario. In this case, we observed a dipolelike structure formed by the manifolds of different chains of hyperbolic points, characterizing an intercrossing scenario when the period of the islands is even.

For the even scenario, the heteroclinic intersections always occur, but this does not mean high transport, as in the odd case. The lobes formed in this scenario are small, decreasing the transport through the phase space. The low and high transport can also be described by the chaotic saddle. The density and the continuity of the chaotic saddle play important roles in the transport: dense and continuous saddles decrease the transport, while subdivided saddles facilitate the transport through phase space.

ACKNOWLEDGMENTS

This research received the support of the Conselho Nacional de Desenvolvimento Científico e Tecnológico (CNPq-Grants No. 309670/2023-3, No. 403120/2021-7, and No. 301019/2019-3) and Fundação de Amparo à Pesquisa do Estado de São Paulo (FAPESP) under Grants No. 2018/03211-6, No. 2022/12736-0, and No. 2023/10521-0. P.J.M. was supported by U.S. Dept. of Energy Contract No. DE-FG05-80ET-53088.

[1] J. Moser, *Stable and Random Motions in Dynamical Systems*, Annals of Mathematics Studies (Princeton University Press, Princeton, NJ, 1973).

[2] J. D. Meiss, Symplectic maps, variational principles, and transport, Rev. Mod. Phys. **64**, 795 (1992).

[3] R. S. MacKay, J. D. Meiss, and I. C. Percival, Stochasticity and transport in Hamiltonian systems, Phys. Rev. Lett. **52**, 697 (1984).

[4] J. D. Meiss, Thirty years of turnstiles and transport, Chaos **25**, 097602 (2015).

[5] V. Rom-Kedar, Transport rates of a class of two-dimensional maps and flows, Physica D **43**, 229 (1990).

[6] R. S. Mackay, J. D. Meiss, and I. C. Percival, Transport in Hamiltonian systems, Physica D **13**, 55 (1984).

[7] W. Horton, H.-B. Park, J.-M. Kwon, D. Strozzi, P. J. Morrison, and D.-I. Choi, Drift wave test particle transport in reversed shear profile, Phys. Plasmas **5**, 3910 (1998).

[8] D. del-Castillo-Negrete and P. J. Morrison, Hamiltonian chaos and transport in quasigeostrophic flows, in *Chaotic Dynamics and Transport in Fluids and Plasmas*, edited by I. Prigogine, Research Trends in Physics (American Institute of Physics, New York, 1993), pp. 181–207.

[9] D. del-Castillo-Negrete and P. J. Morrison, Chaotic transport by Rossby waves in shear flow, Phys. Fluids A **5**, 948 (1993).

[10] W. S. Koon, M. W. Lo, J. E. Marsden, and S. D. Ross, Heteroclinic connections between periodic orbits and resonance transitions in celestial mechanics, Chaos **10**, 427 (2000).

[11] A. Jorba and B. Nicolás, Transport and invariant manifolds near L_3 in the Earth-Moon bicircular model, Commun. Nonlinear Sci. Numer. Simul. **89**, 105327 (2020).

[12] D. F. Escande, From thermonuclear fusion to Hamiltonian chaos, Eur. Phys. J. H **43**, 397 (2018).

[13] D. del Castillo-Negrete, J. M. Greene, and P. J. Morrison, Area preserving nontwist maps: Periodic orbits and transition to chaos, Physica D **91**, 1 (1996).

[14] P. J. Morrison, Magnetic field lines, Hamiltonian dynamics, and nontwist systems, Phys. Plasmas **7**, 2279 (2000).

[15] A. Delshams and R. de la Llave, KAM theory and a partial justification of Greene's criterion for nontwist maps, SIAM J. Math. Anal. **31**, 1235 (2000).

[16] M. Mugnaine, A. C. Mathias, M. S. Santos, A. M. Batista, J. D. Szezech, Jr., and R. L. Viana, Dynamical characterization of transport barriers in nontwist Hamiltonian systems, Phys. Rev. E **97**, 012214 (2018).

[17] M. Mugnaine, A. M. Batista, I. L. Caldas, J. D. Szezech, Jr., and R. L. Viana, Ratchet current in nontwist Hamiltonian systems, Chaos **30**, 093141 (2020).

[18] R. L. Viana, J. D. Szezech, Jr., A. M. Batista, C. V. Abud, A. B. Schelin, M. Mugnaine, M. S. Santos, B. B. Leal, and B. Bartoloni, Transport barriers in symplectic maps, Braz. J. Phys. **51**, 899 (2021).

[19] J. D. Szezech, Jr., I. L. Caldas, S. R. Lopes, R. L. Viana, and P. J. Morrison, Transport properties in nontwist area-preserving maps, Chaos **19**, 043108 (2009).

[20] J. D. Szezech, Jr., I. L. Caldas, S. R. Lopes, P. J. Morrison, and R. L. Viana, Effective transport barriers in nontwist systems, Phys. Rev. E **86**, 036206 (2012).

[21] G. C. Grime, M. Roberto, R. L. Viana, Y. Elskens, and I. L. Caldas, Shearless curve breakup in the biquadratic nontwist map, Chaos, Solitons Fractals **172**, 113606 (2023).

[22] I. L. Caldas, R. L. Viana, C. V. Abud, J. C. D. Fonseca, Z. O. Guimarães Filho, T. Kroetz, F. A. Marcus, A. B. Schelin, J. Szezech, Jr., and D. L. Toufen, Shearless transport barriers in magnetically confined plasmas, Plasma Phys. Controlled Fusion **54**, 124035 (2012).

[23] W. Horton, P. J. Morrison, X. R. Fu, and J. Pratt, Transport with reversed E_r in the GAMMA-10 tandem mirror, Fusion Sci. Technol. **55**, 15 (2009).

[24] G. Tigan and D. Constantinescu, Bifurcations in a family of Hamiltonian systems and associated nontwist cubic maps, Chaos, Solitons Fractals **91**, 128 (2016).

[25] R. E. de Carvalho and A. M. O. De Almeida, Integrable approximation to the overlap of resonances, Phys. Lett. A **162**, 457 (1992).

[26] G. A. Oda and I. Caldas, Dimerized island chains in tokamaks, Chaos, Solitons Fractals **5**, 15 (1995).

[27] G. Corso and F. B. Rizzato, Manifold reconnection in chaotic regimes, Phys. Rev. E **58**, 8013 (1998).

[28] D. del-Castillo-Negrete, J. M. Greene, and P. J. Morrison, Renormalization and transition to chaos in area preserving nontwist maps, Physica D **100**, 311 (1997).

[29] E. Petrisor, Nontwist area preserving maps with reversing symmetry group, Int. J. Bifurcation Chaos **11**, 497 (2001).

[30] A. C. Mathias, M. Mugnaine, M. S. Santos, J. D. Szezech, Jr., I. L. Caldas, and R. L. Viana, Fractal structures in the parameter space of nontwist area-preserving maps, Phys. Rev. E **100**, 052207 (2019).

[31] J. D. Meiss, Average exit time for volume-preserving maps, Chaos **7**, 139 (1997).

[32] E. G. Altmann, J. S. E. Portela, and T. Tél, Leaking chaotic systems, Rev. Mod. Phys. **85**, 869 (2013).

[33] E. G. Altmann, A. E. Motter, and H. Kantz, Stickiness in Hamiltonian systems: From sharply divided to hierarchical phase space, Phys. Rev. E **73**, 026207 (2006).

[34] J. D. Meiss and E. Ott, Markov tree model of transport in area-preserving maps, Physica D **20**, 387 (1986).

[35] G.-H. Hsu, E. Ott, and C. Grebogi, Strange saddles and the dimensions of their invariant manifolds, Phys. Lett. A **127**, 199 (1988).

[36] H. E. Nusse and J. A. Yorke, A procedure for finding numerical trajectories on chaotic saddles, Physica D **36**, 137 (1989).

[37] J. D. Farmer, E. Ott, and J. A. Yorke, The dimension of chaotic attractors, Physica D **7**, 153 (1983).

Correction: The previously published Figure 4 contained a missing panel and has been replaced.